Chinese Chemical Letters 33 (2022) 3291–3295

Contents lists available at ScienceDirect

Chinese Chemical Letters

journal homepage: www.elsevier.com/locate/cclet

Dual-metal zeolite imidazolate framework for efficient lithium storage boosted by synergistic effects and self-assembly 2D nanosheets

Ming Yue[a], Yajing Fu[a], Canping Zhang[a], Junxiao Fu[a], Shiquan Wang[a,*], Jianwen Liu[a,b,*]

[a] *College of Chemistry and Chemical Engineering & Collaborative Innovation Center for Advanced Organic Chemical Materials Co-constructed by the Province and Ministry & Ministry of Educational Key Laboratory for the Synthesis and Application of Organic Functional Molecules, Hubei University, Wuhan 430062, China*

[b] *Jiangsu Pylon Battery Co., Ltd., Yangzhou 211400, China*

ARTICLE INFO

Article history:
Received 22 August 2021
Revised 22 November 2021
Accepted 6 December 2021
Available online 12 December 2021

Keywords:
Lithium ion batteries
Metal-organic frameworks
CoCu-ZIF nanosheets
Synergistic effect
Self-assembly

ABSTRACT

Metal-organic framework materials (MOFs), such as zeolitic imidazolate framework (ZIF), have been widely used in energy storage due to their advantages such as high structural stability, large specific surface, more active sites and skeleton structures. Herein, a novel two-dimensional (2D) CoCu-ZIF was synthesized by a facile solvothermal method. The as-prepared CoCu-ZIF nanosheets exhibit an ultrahigh reversible capacity of 2287.4 mAh/g and remains at 1172.1 mAh/g after 300 cycles at a current density of 100 mA/g, far better than that of the single Co-ZIF and Cu-ZIF. Additionally, the specific discharge capacity of CoCu-ZIF nanosheets can maintain at about 590 mAh/g after 1000 cycles at the current density of 2 A/g. Owing to the synergistic effect of two metals, function of nitrogen in the molecular and self-assembly 2D nanosheets, our research can provide strong support for the practical application of CoCu-ZIF materials in lithium ion batteries.

Lithium ion batteries (LIBs) have attracted extensive attention as a most useful battery system for portable devices in recent years, owing to the relatively high theoretical specific capacity and excellent cycling performance [1–4]. However in order to solve the problem of large volume variation and poor electrical conductivity of high energy density electrode materials, it is imminent to search suitable anode materials [5–7]. For example, graphene [8,9], Mxenes [10,11], black phosphorus [12,13], two-dimensional transition metal sulfide (TMDs) and other traditional 2D materials [14–16] gradually show structural advantages. Especially, due to the significant advantages of light weight, good electron and ion conductivity, rich pores and uniform distribution of active sites, metal-organic frameworks (MOFs) have been considered as superior anode materials [17–28]. In Li's review, transition-metal (Zn, Mn, Cu)-based MOFs as anode materials and their strategies for further enhancing performance in LIBs were proposed [29]. Wang *et al.* reported four polyoxometalate-based metal-organic frameworks (POMOFs) with various architectures employed in anode materials of LIBs [30]. Jin *et al.* designed a 2D few layer black phosphorous/NiCo (BP/NiCo) MOF structure with high reversible capacity, long cycle life and excellent rate capability [31]. The bimetallic zeolite imidazolate framework CoZn-ZIF delivered a high reversible capacity of 605.8 mAh/g at a current density of 100 mA/g, far beyond the performance of the corresponding monometallic Co-ZIF-67 and Zn-ZIF-8 [32].

In our work, CoCu-ZIF composites were prepared through layer-by-layer stacking of 2D nanosheets by a facile solvothermal method. These nanosheets are stacked together in an orderly way, which effectively inhibits the volume change and accelerates the transport of lithium ions. Additionally, the synergistic effect of dual-metals can significantly improve the electrochemical performance of the electrode material with practical value. As a consequence, CoCu-ZIF nanaosheets with multilayer structure display excellent electrochemical properties in LIBs, which is superior to the MOFs materials previously reported.

In a one-step solvothermal reaction as illustrated in Fig. S1 (Supporting information), 0.46 g $Cu(NO_3)_2 \cdot 3H_2O$ and 0.96 g $Co(NO_3)_2 \cdot 6H_2O$ ($n_{Co}:n_{Cu} = 1.2:1$) were dissolved in 44 mL 75% ethanol for stirring to obtain solution A and B, respectively. Then the solution A was poured into the solution B for magnetic stirring for 10 h to obtain mixed solution. 1.0 g 2-methylimidazole (2-Im) was dissolved in 88 mL 75% ethanol to obtain mixed solution with the above solution. Subsequently, this mixed solution was transferred into a 100 mL teflon-lined stainless steel autoclave and heated for 12 h at 100 °C in the oven. After the reaction, it was

---

* Corresponding authors.
E-mail addresses: wsqhao@hubu.edu.cn (S. Wang), jianwen@hubu.edu.cn (J. Liu).

https://doi.org/10.1016/j.cclet.2021.12.015

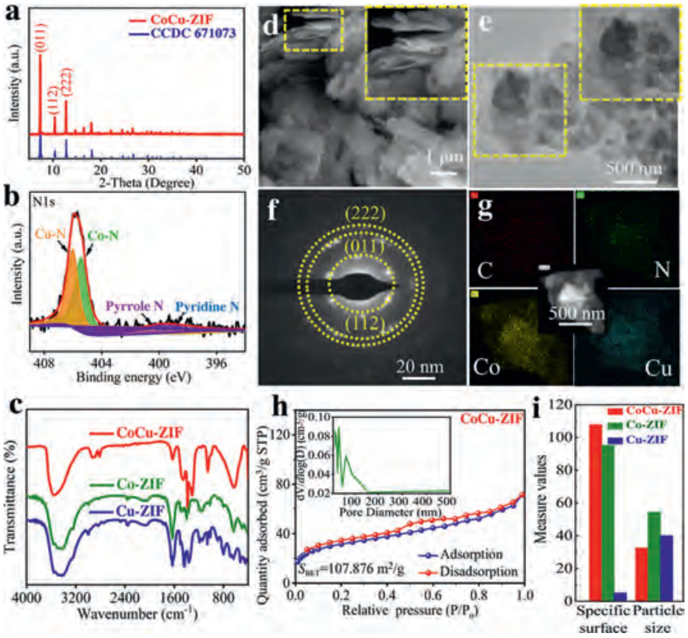

Fig 1. (a) XRD patterns and (b) N 1s high-resolution XPS spectrum of CoCu-ZIF sample. (c) FTIR spectra of CoCu-ZIF, Co-ZIF or Cu-ZIF samples. (d) FE-SEM images, (e) TEM images, (f) electronic diffraction (ED) and (g) elemental mapping of CoCu-ZIF sample (The insets are the local enlargement figures). (h) Nitrogen adsorption/desorption isotherms and pore-size distribution of CuCo-ZIF sample and (i) its comparison with Co-ZIF and Cu-ZIF samples.

naturally cooled to room temperature, and the yellow product was obtained by centrifugation, washing with deionized water for three times. Finally, the yellow product CoCu-ZIF was dried overnight in a vacuum oven at 60 °C. For comparison, the same procedures were carried out to synthesize Co-ZIF and Cu-ZIF without using $Cu(NO_3)_2{\cdot}3H_2O$ or $Co(NO_3)_2{\cdot}6H_2O$, respectively.

Fourier transform-infrared spectroscopy (FTIR, SHIMADZU) measurements were performed within the wavenumber range of $4000{\sim}400$ cm^{-1}. The X-ray diffractometer (XRD, Bruker D8 Advance) with Cu Kα radiation source was used to analyze the crystal phase of the as-prepared materials in the 2θ range of $5°–50°$ The chemical status of elements were determined by X-ray photoelectron spectroscopy (XPS, Thermo escalab 250Xi systerm). The field-emission scanning electron microscopy (FE-SEM) images were observed by a JSM-7800F & TEAM Octane Plus (Japan). Transmission electron microscopy (TEM) and high resolution TEM (HRTEM) images were tested on a TecnaiF20 device. The Brunauer-Emmett-Teller (BET) tests were carried out on a Micromeritics ASAP 2020 porosimetry system. For assembling the batteries, active material, conductive additive (super-P carbon black) and the binder (polyvinylidene tetrafluoroethylene, PVDF) with the weight ratio of 7:2:1 were mixed in *N*-methyl-2-pyrrolidone (NMP, solvent) to form a homogeneous slurry. All the working electrode, diaphragm, electrolyte (1.0 mol/L $LiPF_6$ in ethylene carbonate (EC) and diethyl carbonate (DEC) with a volume ratio of 1:1) and lithium foil were used to manufacture CR2035 coin cells in an Ar glove box. The galvanostatic charge and discharge cycles were tested using automatic battery testing system (Neware, China) within the voltage range from 0.01 V to 3.0 V (*vs.* Li^+/Li). Cyclic voltammetry (CV) curves were recorded from 0.01 V to 3.0 V at a scanning rate of 0.2 mV/s using an electrochemical workstation (CHI660E). Electrochemical impedance spectroscopies (EIS) were tested applying an AC voltage of 0.1 mV within a frequency range of 0.01 Hz to 100 kHz.

Fig. 1a and Fig. S2 (Supporting information) display the XRD patterns of CoCu-ZIF, Co-ZIF and Cu-ZIF samples. Owing to the approximate ionic radius of Co^{2+} (0.73 Å) and Cu^{2+} (0.72 Å), $Co^{2+}$and Cu^{2+} ions can be simutaneously coordinated with 2-methylimidazole to form isostructure CoCu-ZIF composites [32–34]. To be specific, the strong and sharp peaks observed at 7.46°, 10.35° and 12.69° in Fig. S2, which are consistent with the simulated ZIF-67 (CCDC No. 671,073), confirm a high degree of crystallinity of Co-ZIF samples [29,35-39]. Additionally, the strong peaks recorded at 7.43°, 10.38° and 12.72° for CoCu-ZIF perfectly match well with (011), (112) and (222) lattice plane in Fig. 1a, proving that CoCu-ZIF composite is successfully synthesized via the coordination of Co^{2+} and Cu^{2+}ions with 2-Im. It must be pointed out here that the angular shifts in XRD patterns of bimetallic complex are mainly due to the introduction of Cu metal.

In the high-resolution XPS spectra of CoCu-ZIF shown in Fig. 1b and Fig S3 (Supporting information), the typical characteristic peaks of N 1s, C 1s, O 1s, Co 2p and Cu 2p can be all observed. First, the N 1s spectra exhibit significant peaks at 397.4, 399.6, 405.4 and 406 eV corresponding to pyridine nitrogen, pyrrole nitrogen, Co-N, and Cu-N bonds respectively, which confirms the successful coordination of Cu and Co onto ZIF skeleton [33]. In C 1s spectra, there are four strong peaks located around 283.9, 284.3, 285.2 and 288.1 eV belonging to C–C, C–N, C=O and O–C=O bonds, respectively. The C=O and O-C=O bonds could be caused by the partial oxidation of material surface or the adsorption of water [29]. The Co 2p spectra are divided into four peaks at 780 and 785.5 eV from Co^{3+} and Co^{2+} respectively, and followed by 796.6 and 802.7 eV as their corresponding satellite peaks. Similarily, the Cu 2p spectra display two strong peaks at 934.2 and 935.4 eV corresponding to Cu^+ and Cu^{2+}, respectively, and their satellite peaks at the binding energy of 939.8 and 943 eV.

In the FTIR spectra of Co-ZIF, Cu-ZIF and CoCu-ZIF samples displayed in Fig. 1c, the characteristic bands of 2-methylimidazole are not observed at 1846 cm^{-1} (the resonance between $\gamma_{N-H\cdots N}$ and υ_{N-H} proton tensile vibration out of plane) and at 2300–3300 cm^{-1} (the establishment of N–H···N hydrogen bond between two 2-methylimidazoles), revealing the deprotontion of 2-methylimidazole with metals after successful coordination [32,40]. It is worthy noted that the N atoms in the molecular have been all participated in the coordination with Co or Cu metal *via* deprotontion of 2-methylimidazole, thus resulting in no appearance of N–H groups. Therefore, we confirm that the very strong and wide peak at 3440 cm^{-1} corresponds to the stretching vibration of O–H groups [32,33,40,41]. Additionally, owing to the coordination of Co^{2+} and Cu^{2+} with all N atoms in 2-methylimidazoles, the wide peak of CoCu- ZIF moves towards high wavenumbers around 3531 cm^{-1} [30].

In the SEM images shown in Fig. 1d, the as-prepared CoCu-ZIF is mainly composed of scattered nanosheets assembled by a large number of thin sheets layer by layer. The particle surface presents very flat and smooth, which can greatly slow down volume expansion during charge and discharge process. By comparison, the SEM images of Co-ZIF and Cu-ZIF in Fig. S4 (Supporting information) display embroidered globular and blocky morphology, respectively. The TEM images of CoCu-ZIF observed in Fig. 1e also show the characteristics of thick accumulation and thin sheets in the edge. This unique structure can improve the specific surface area, which promotes electron transfer and enhances the electrochemical performance of CoCu-ZIF electrode. Moreover, the electronic diffraction (ED) shown in Fig. 1f exhibits (011), (112), (222) lattice plane, which results are consistent with the XRD patterns. As depicted in Fig. 1g, the corresponding element mapping proves that Co, Cu, C and N are uniformly distributed in whole CoCu-ZIF nanosheets.

For evaluating the physical property of the as-prepared samples, the BET test was perfomed as shown in Figs. 1h and i and Fig. S5 (Supporting information). The specific surface areas of CoCu-ZIF, Co-ZIF and Cu-ZIF samples are 107.86, 95.315 and 5.195 m^2/g,

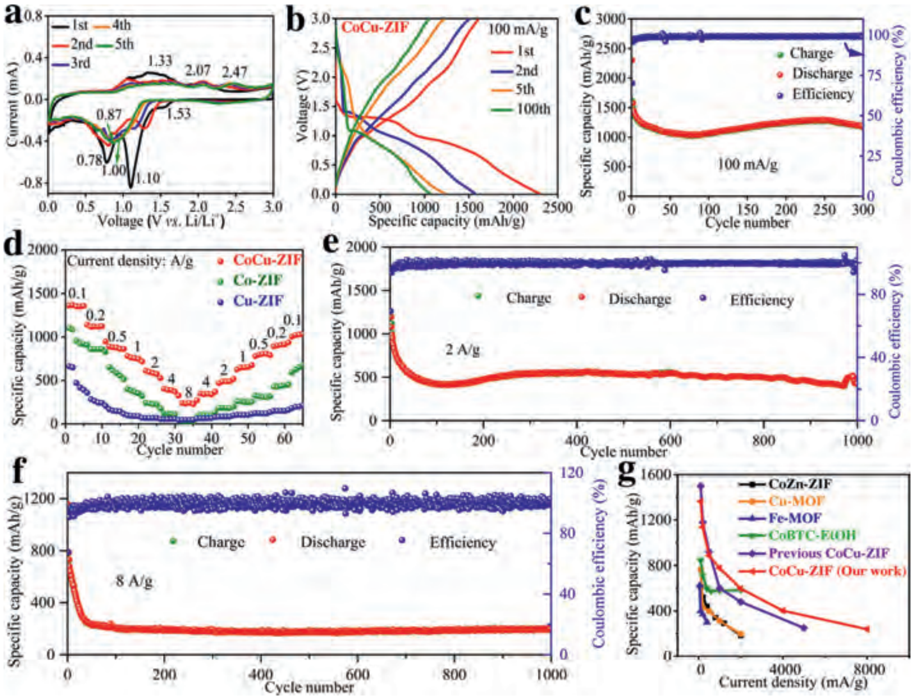

Fig 2. (a) CV curves, (b) selected charge-discharge profiles and (c) cycling performance at 0.1 A/g of CoCu-ZIF samples. (d) Rate capability of CoCu-ZIF, Co-ZIF and Cu-ZIF samples. Long cycling performance of CoCu-ZIF samples at the current densities of (e) 2 A/g and (f) 8 A/g. (g) Comparison of our work with other MOFs materials reported previously.

respectively. The CoCu-ZIF has the largest specific surface area because it is composed of thin nanosheets. According to the pore size distributions of 32.68 nm, it implies that the as-prepared CoCu-ZIF in our work is a typical mesoporous material with the advantages of regular pore structure and good structural stability.

In order to investigate the electrochemical properties of CoCu-ZIF, Co-ZIF and Cu-ZIF electrodes, the cyclic voltammetry (CV) curves are displayed in Fig. 2a and Fig. S6 (Supporting information). In the lithiation process of first cycle, there is a typical peak at 1.53 V which could be attributed to the Li^+ insertion into $Co(2\text{-}Im)_2$ and $Cu(2\text{-}Im)_2$ to form Cu(2-Im)Li and Co(2-Im)Li (as illustrated in Eqs. 1 and 2) [31]. The weak reduction peaks located at 1.10 and 0.78 V might be originated from the formation of solid electrolyte interphase (SEI) and the reduction of $Co_xCu_{(1\text{-}x)}(2\text{-}Im)_2$ to $Co_xCu_{(1\text{-}x)}(2\text{-}Im)_2Li_4$ (Eq. 3) [32]. In the cathode scanning of first circle, the two main oxidation peaks around 1.33 and 2.07/2.47 V are mainly derived from the oxidation reaction of Co and Cu to form Co^{2+} and Cu^{2+}, respectively. It is can be obviously observed that from the fourth cycle on the CV curves overlap well, proving that the CoCu-ZIF nanosheets exhibit better stability. The reaction mechanism of CoCu-ZIF nanosheets during charge and discharge process can be explained as the following equations.

$$Cu(2\text{-}Im)_2 + Li^+ + e^- \leftrightarrow Cu(2\text{-}Im)Li \quad (1)$$

$$Co(2\text{-}Im)_2 + Li^+ + e^- \leftrightarrow Co(2\text{-}Im)Li \quad (2)$$

$$Co_xCu_{(1\text{-}x)}(2\text{-}Im)_2 + 4Li^+ + 4e^- \leftrightarrow Co_xCu_{(1\text{-}x)}(2\text{-}Im)_2Li_4 \quad (3)$$

The battery performances of CoCu-ZIF, Co-ZIF and Cu-ZIF samples in the voltage range of 0.01~3.0 V are displayed in Fig. 2 and Fig. S7 (Supporting information). These three electrodes deliver very satisfactory initial discharge specific capacities of 2287.4, 1882.9 and 1924.3 mAh/g, respectively. For most MOFs electrode materials, the discharge specific capacity of second cycle is obviously reduced due to irreversible side reactions, SEI formation and electrolyte decomposition [42]. Obviously, the Co-ZIF and Cu-ZIF electrodes appear significant capacity decline and maintain the low capacity cyclings. By contrast, the capacity of CoCu-ZIF nanaosheet displays a trend of decreasing first and rising then, and maintains a very stable state after dozens of cycles. For example, the specific capacity of CoCu-ZIF nanosheet remains at 1172.1 mAh/g after 300 cycles at the current density of 100 mA/g. Additionally, the specific discharge capacities of CoCu-ZIF nanosheets can still maintain at about 590 and 290 mAh/g after 1000 cycles at the current densities of 2 and 8 A/g, respectively. For the rate capability, the CoCu-ZIF nanosheet presents the reversible capacities of 1365.1, 1138, 887.1, 777.1, 595.7, 401.9 and 238.6 mAh/g at the current densities of 100, 200, 500, 1000, 2000, 4000 and 8000 mA/g, respectively. When the current density returns to 100 mA/g, the capacity still recover and remain at about 1005.9 mAh/g. Therefore, these results reveal that the CoCu-ZIF nanosheets has better cyclic performance and rate stability than Co-ZIF and Cu-ZIF samples. Owing to the synergistic effect of bimetallic ZIF, the CoCu-ZIF nanosheets in this work behave the excellent electrochemical performance, which much better than those in many previous reports shown in Fig. 2g and Table S1 (Supporting information) [32,41,43-45].

To understand the reaction kinetics of electrode materials, the EIS impedance profiles of CoCu-ZIF, Co-ZIF and Cu-ZIF samples are shown in Figs. 3a and b. Firstly, the R_{ct} values of CoCu-ZIF, Co-ZIF and Cu-ZIF electrodes are 45.19, 64.99 and 128.60 Ω respectively, which confirms that the bimetallic electrode material has the best conductive performance. Secondly, the slopes of impedance Z' (Ohm) against the angular frequency $\omega^{-1/2}$ of these three electrodes display 22.07, 33.49 and 70.14, respectively. Using the following Eqs. 4 and 5, the lithium ion diffusion coefficient (D_{Li^+}) are calculated as 7.01×10^{-11}, 3.04×10^{-11} and 6.94×10^{-12} cm/s, respectively. It is proved that CoCu-ZIF nanosheet behaves the fastest reaction kinetics and excellent lithium ion transport and diffusion ability [46–48].

$$Z' = R_s + R_{ct} + A_w\omega^{-1/2} \quad (4)$$

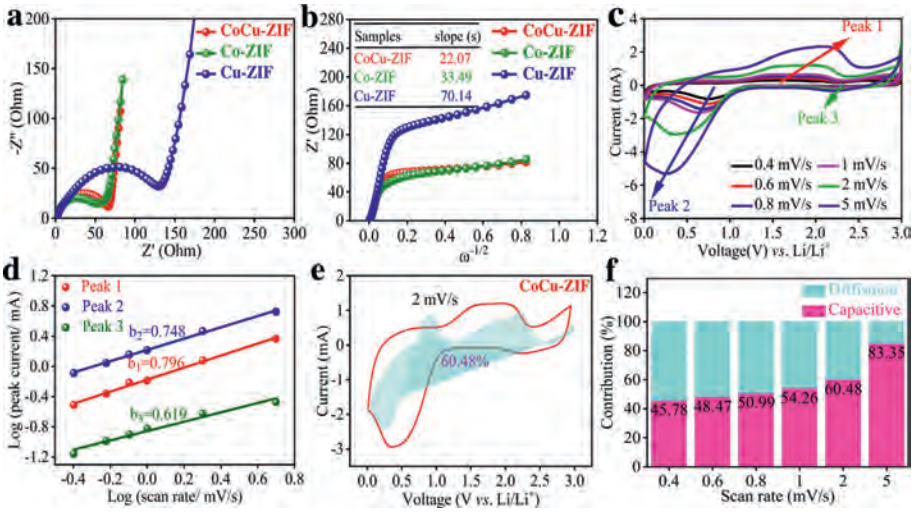

Fig 3. (a) Nyquist plots and (b) liner fitting of Z' *vs.* $\omega^{-1/2}$ in all-frequency region of the CoCu-ZIF nanosheets. (c) CV curves of the CoCu-ZIF nanosheets at different scan rate of 0.4–5.0 mV/s. (d) Calculation of b values by plotting log$i$ *versus* logυ. (e) Contribution of diffusion and pseudocapacitive-controlled capacity at the scan rate of 2 mV/s. (f) Contribution percentage of pseudocapacitive-controlled capacity at different scan rates of 0.4~5.0 mV/s.

$$D(\mathrm{Li}^+) = \mathrm{R}^2T^2/(2A^2n^4F^4C^2\sigma^2) \tag{5}$$

In order to further explore the electrochemical properties and charge-discharge storage mechanism of CoCu-ZIF nanosheets, CV curves were measured at different scanning rates to evaluate the electrochemical dynamics and capacitive capacity. The CV curves of CoCu-ZIF nanosheets at different scanning rates of 0.4, 0.6, 0.8, 1, 2 and 5 mV/s over the potential 0.01–3.0 V (*vs.* Li/Li$^+$) are displayed in Fig. 3c. For the electrode material, the value of b can be calculated by Eq. 6 (i represents peak current value; υ represents different scanning rates) to determine whether there is pseudocapacitance behavior in the process of charge and discharge. Generally, if the value of b is within the range of 0.5–1, the electrode material exhibits both battery and pseudocapacitance properties; if the value of b is greater than or equal to 1, the electrode material exhibits pseudocapacitance properties [49,50]. By linear fitting of log$i$ and logυ from Eq. 7, the value of b (slope) can be obtained. As presented in the Fig. 3d, the calculated and fitted values of b_1, b_2 and b_3 are 0.796, 0.748 and 0.619 respectively, which reveals that the capacitance of CoCu-ZIF nanosheets is composed of pseudocapacitance contribution and diffusion control contribution [49,50]. When the CV scanning rate of CoCu-ZIF nanosheets reaches 2 mV/s, the contribution rate of the pseudocapacitance reaches 60.48% in Fig. 3e through calculation of Eq. 8. Moreover, as the CV scanning rate gradually increases, the proportion of pseudocapacitive behavior also increases in Fig. 3f. The highest pseudocapacitance contribution (83.35%) can be obtained when the scanning rate of CV reaches 5.0 mV/s. This result indicates that the CoCu-ZIF material has high pseudocapacitive behavior and exhibits excellent electrochemical capability [51].

$$i = a\upsilon^b \tag{6}$$

$$\log i = \log a + b\log\upsilon \tag{7}$$

$$i/\upsilon^{1/2} = k_1\upsilon^{1/2} + k_2 \tag{8}$$

Based on the above results and related analysis, the mechanism of CoCu-ZIF nanosheets for enhanced electrochemical performance can be illustrated as Fig. 4. First, the better electrochemical performance of dual-metal MOFs than mono-metal MOFs could be mainly attributed to lithiation and delithiation of nitrogen atoms, accompanied by the breakage and recoordination of metal nitrogen bond. Morever, a few metal nitrogen bonds without recoordination could lead to the amorphization of CoCu-ZIF and the generation of few nitrogen radicals [16,18,19]. Second, Co and Cu metals both have multiple valence states, and with the similar metal activity. Cu(II) has an electron configuration of d9 and can form stable coordination compounds from common ligands with coordination number of 2, 4 and 6, such as $[\mathrm{Cu(NH_3)_4}]^{2+}$, $[\mathrm{Cu(NH_3)_4(H_2O)_2}]^{2+}$. Meanwhile, Co(II) can also form stable complexes with common ligands, such as $[\mathrm{Co(H_2O)_6}]^{2+}$, $[\mathrm{Co(NH_3)_6}]^{2+}$, $[\mathrm{Co(CN)_6}]^{4-}$, $[\mathrm{Co(NCS)_4}]^{2-}$. Additionally, Co^{2+} (0.73 Å) and Cu^{2+} (0.72 Å) have the very close ion radius. Therefore, the two metals with similar properties (Co and Cu) are more likely to play a synergistic role, which is more beneficial to battery performance [22,23]. As for the function of nitrogen element, it can directly participate in the redox reactions and the formation of dense SEI film on the electrode in the process of battery charge and discharge [31,32,42]. Besides, the as-synthesized unique CoCu-ZIF nanosheets in our work can provide more active sites, fast electron and ion transport channels, which can greatly improve the performance of battery. Therefore as shown in the figure, the surface of electrode after 300 cycles still presents an integrated and stable structure.

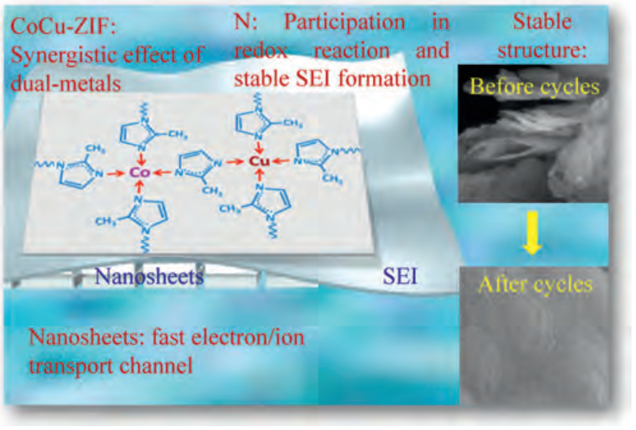

Fig 4. Illustration of mechanism of CoCu-ZIF nanosheets for enhanced electrochemical performance.

In summary, a novel 2D CoCu-ZIF nanosheet was synthesized by a facile solvothermal method. When applied as anode material for LIBs, the CoCu-ZIF nanosheets display better electrochemical performance including cycling stability and rate performance, compared with the single Co-ZIF and Cu-ZIF. For example, the as-prepared CoCu-ZIF nanosheets exhibit an ultrahigh reversible capacity of 2287.4 mAh/g and remain at 1172.1 mAh/g after 300 cycles at a current density of 100 mA/g. Additionally, the specific discharge capacity of CoCu-ZIF nanosheets can maintain at about 590 and 290 mAh/g after 1000 cycles at the current densities of 2 and 8 A/g, respectively. Until now, the battery performance in our work is superior to other bimetallic materials reported previously. These excellent electrochemical properties can be attributed to the synergistic effect of two metals, function of nitrogen in the molecular and self-assembly 2D nanosheets. This research in our study will provide support for the practical application of anode materials for lithium ion batteries.

Declaration of competing interest

The authors declare that they have no known competing financial interests or personal relationships that could have appeared to influence the work reported in this paper.

Acknowledgments

The authors are very grateful for the finacial support from the National Natural Science Foundation of China (Nos. 21978073 and U1903217) and the Project of Hubei Provincial Science & Technology Department (No. 2018ACA147). The authors would also like to thank the Analytical and Testing Center of Hubei University for providing the facilities to fulfill the experimental measurements. The technical supports from Jiangsu Pylon Battery Co., Ltd. are also gratefully acknowledged.

Supplementary materials

Supplementary material associated with this article can be found, in the online version, at doi:10.1016/j.cclet.2021.12.015.

References

[1] F. Duffner, N. Kronemeyer, J. Tübke, et al., Nat. Energy 6 (2021) 123–134.
[2] C. Zhang, L. Shen, J.Q. Shen, et al., Adv. Mater. 31 (2019) 1808338.
[3] J.W. Liu, D.X. Xie, W. Shi, et al., Chem. Soc. Rev 49 (2020) 1624–1642.
[4] J.W. Liu, D.X. Xie, X.F. Xu, et al., Nat. Commun. 12 (2021) 3131.
[5] Q. Cai, Y. Li, L. Wang, et al., Nano Energy 32 (2016) 1–9.
[6] Y. Na, X.H. Sun, A. Fan, S. Cai, C.M. Zheng, Chin. Chem. Lett. 32 (2021) 973–982.
[7] S. Jaekyung, J.Y. Ma, S.H. Choi, et al., Adv. Mater. 31 (2019) 1900970.
[8] W. Wei, F.F. Jia, K.F. Wang, et al., Chin. Chem. Lett. 28 (2017) 324–328.
[9] R.P. Fang, K. Chen, L.C. Yin, et al., Adv. Mater. 31 (2019) 1970066.
[10] C.L. Wei, Y. Tao, Y.L. An, et al., Adv. Funct. Mater. 30 (2020) 2004613.
[11] F. Ming, H. Liang, G. Huang, et al., Adv. Mater. 33 (2020) 2004039.
[12] J.P. Zhu, G.S. Xiao, X.X. Zuo, Nano-Micro Lett. 12 (2020) 3699.
[13] I. Sultana, M.M. Rahman, T. Ramireddy, et al., J. Mater. Chem. A 5 (2017) 23506–23512.
[14] Y. Liu, C. Yang, Q. Zhang, et al., Energy Storage Mater. 22 (2019) 60–95.
[15] P. Geng, S. Zheng, H. Tang, et al., Adv. Energy Mater. 8 (2018) 1703259.
[16] Y.J. Li, S.J. Guo, Matter 4 (2021) 1142–1188.
[17] C. Li, L. Liu, J.L. Kang, et al., Energy Storage Mater 31 (2020) 15–134.
[18] E.M. Miner, S.S. Park, M. Dinca, J. Am. Chem. Soc. 141 (2019) 4422–4427.
[19] L. Shen, H.B. Wu, F. Liu, et al., Adv. Mater. 30 (2018) 1707476.
[20] G. Zou, H. Hou, P. Ge, et al., Small 14 (2018) 1702648.
[21] H.Q. Jiang, X.C. Liu, Y. Wu, et al., Angew. Chem. Int. Ed. 57 (2018) 3916–3921.
[22] Y.L. Li, B.M. Jia, Y.Z. Fan, et al., Adv. Energy Mater. 8 (2018) 1702048.
[23] Y.L. Jia, F.S. Zhang, Q.L. Liu, et al., Chin. Chem. Lett. 33 (2022) 1070–1073.
[24] Y. Li, Y.X. Xu, W.P. Yang, et al., Small 14 (2018) 1704435.
[25] Y.F. Gu, Y.N. Wu, S. Kitagawa, et al., Angew. Chem. Int. Ed. 129 (2017) 15864–15868.
[26] D. Yin, G. Huang, Z. Na, et al., ACS Energy Lett. 2 (2017) 1564–1570.
[27] R. Zhao, Z.B. Liang, R.Q. Zou, et al., Joule 2 (2018) 2235–2259.
[28] Q. Huang, T. Wei, M. Zhang, et al., J. Mater. Chem. A 5 (2017) 8477–8783.
[29] T. Li, Y.W. Y.L.Bai, et al., Coordin. Chem. Rev. 410 (2020) 213221.
[30] Z.K. Wang, R. Bi, J.D. Liu, et al., Chen. Eng. J. 404 (2021) 127117.
[31] J. Jin, Y. Zheng, S.Z. Huang, et al., J. Mater. Chem. A 7 (2019) 783–790.
[32] X.B. Lou, Y. Ning, L.C. Li, et al., Sci. China Mater. 61 (2018) 1040–1048.
[33] Y. Liu, S.J. Huang, J.N. Li, et al., Microchim. Acta 188 (2021) 69.
[34] W.R. Zheng, M.J. Liu, L.Y. Lee, ACS Catal. 10 (2020) 81–92.
[35] C. Liu, X.D. Huang, J.Z. Liu, et al., Adv. Sci. 7 (2019) 1901480.
[36] Z.H. Wang, H.H. Jin, T. Meng, et al., Adv. Funct. Mater. 28 (2018) 1802596.
[37] Q.X. Lai, J.J. Zhu, Y.X. Zhao, et al., Small 13 (2017) 1700740.
[38] Y.W. Zhang, S.N. Yun, M.L. Sun, et al., J. Colloid Interf. Sci. 604 (2021) 441–457.
[39] J. Cui, J.M. Liu, C.B. Wang, et al., Electrochim. Acta 334 (2020) 135577.
[40] G.C. Li, W. Zhao, J. Alloy. Compd. 716 (2017) 156–161.
[41] W. Chen, Y.M. Jia, X.F. Yu, et al., Ionics (Kiel) 26 (2020) 2107–2115.
[42] A. Nazir, H. Le, A. Kasbe, C.J. Park, Chem. Eng. J. 405 (2021) 126963.
[43] Y. Luo, M. Wu, B. Pang, et al., ChemistrySelect 5 (2020) 4160–4164.
[44] Y. Jin, C. Zhao, Z. Sun, et al., RSC Adv. 6 (2016) 30763–30768.
[45] C. Li, X. Lou, M. Shen, et al., ACS Appl. Mater. Inter. 8 (2016) 15352–15360.
[46] G.T. Xiang, J.M. Yin, X.X. Zhang, et al., Chin. Chem. Lett. 32 (2021) 2169–2173.
[47] J.C. Zheng, Z. Yang, Z.J. He, et al., Nano Energy 53 (2018) 613–621.
[48] J.F. Zhu, J. Chen, H. Xu, et al., ACS Appl. Mater. Inter. 11 (2019) 17384–17392.
[49] S. Shi, C. Sun, X. Yin, et al., Adv. Funct. Mater. 30 (2020) 1909283.
[50] S.F. Jiang, S. Huang, M.J. Yao, et al., Chin. Chem. Lett. 31 (2020) 2347–2352.
[51] L.T. Yu, L.G. Zhang, K.H. Kim, et al., Chem. Eng. J. 417 (2021) 129106.